

Heavy Magnetic Neutron Stars

Ishfaq A. Rather¹, Usuf Rahaman¹, V. Dexheimer², A. A. Usmani¹, and S. K. Patra^{3,4}

¹ Department of Physics, Aligarh Muslim University, Aligarh 202002, India
e-mail: ishfaqrather81@gmail.com

² Department of Physics, Kent State University, Kent OH 44242 USA

³ Institute of Physics, Bhubaneswar 751005, India

⁴ Homi Bhabha National Institute, Training School Complex, Anushakti Nagar, Mumbai 400094, India

ABSTRACT

Context.

Aims. We systematically study the properties of pure nucleonic and hyperonic magnetic stars using a density-dependent relativistic mean field (DD-RMF) equations of state.

Methods. We explore several parameter sets and hyperon coupling schemes within the DD-RMF formalism. We focus on sets that agree with nuclear and other astrophysical data, while generating heavy neutron stars. Magnetic field effects are included in the matter equation of state and in general relativity solutions, which in addition fulfill Maxwell's equations.

Results. We find that pure nucleonic matter, even without magnetic field effects, generates neutron stars that satisfy the potential GW190814 mass constraint; however, this is not the case for hyperonic matter, which instead only satisfies the more conservative $2.1 M_{\odot}$ constraint. In the presence of strong but still realistic internal magnetic fields $\approx 10^{17}$ G, the stellar charged particle population re-leptonizes and de-hyperonizes. As a consequence, magnetic fields stiffen hyperonic equations of state and generate more massive neutron stars, which can satisfy the possible GW190814 mass constraint but present a large deformation with respect to spherical symmetry.

Key words. Equation of State – Magnetic fields – Neutron stars

1. Introduction

Neutron stars (NSs) are considered to be the densest objects that are formed as a result of the gravitational collapse of supernovae. Their interior covers a wide range of densities (reaching ~ 10 times the normal nuclear density) and, hence, invites the possibility of exotic degrees of freedom like quarks, hyperons, and kaons. They also provide a distinctive environment to investigate many unknowns in physics and astrophysics. The properties of the interior dense matter affect NS macroscopic properties, such as mass, radius, and the amount by which it can be deformed.

The most precise measurement of a NS mass is $1.4 M_{\odot}$, that of the Hulse-Taylor pulsar (Hulse & Taylor 1975). Recently, higher masses of binary neutron-star (BNS) systems like millisecond pulsar (MSP) PSR J1614-2230 ($M = 1.97 \pm 0.04 M_{\odot}$) (Demorest et al. 2010), PSR J0348+0432 ($M = 2.01 \pm 0.04 M_{\odot}$) (Antoniadis & Freire et al. 2013), and PSR J0740+6620 ($M = 2.04^{+0.10}_{-0.09} M_{\odot}$) (Cromartie & Fonseca et al. 2019) have been measured with high precision. The gravitational wave detection by LIGO and Virgo Collaborations (LVC) of a BNS merger GW170817 event (Abbott et al. 2017, 2018) further provided a precise measurement of the NS mass, $1.16\text{--}1.60 M_{\odot}$ for low spin priors and a maximum mass approaching $1.9 M_{\odot}$ for high spin priors (Abbott et al. 2019), which allowed one to study dense matter properties at extreme conditions due to the measurement of a new property of NSs, the tidal deformability. The latter provided a new constraint on the NS EoS and its variation with the radius approximated by the relation $\Lambda \propto R^5$ (Hinderer et al. 2010; Kumar et al. 2017) resulting in a strong constraint on the nuclear EoS at intermediate density.

Very recently, a new gravitational wave event reported by LVC as GW190814 (Abbott et al. 2020) was observed with a $22.2\text{--}24.3 M_{\odot}$ black hole and $2.50\text{--}2.67 M_{\odot}$ secondary component. The secondary component of GW190814 attracted a lot of attention as it contained no measurable tidal deformability signatures. As the mass of the secondary component of GW190814 lies in the lower region of the mass-gap ($2.5 M_{\odot} < M < 5 M_{\odot}$), it raised the question whether it is a light black hole or a very massive NS. To understand this object, many interesting theories have been proposed recently regarding its nature as the most massive NS, lightest black hole, or fastest pulsar (Godzieba et al. 2021; Most et al. 2020; Zhang & Li 2020; Tsokaros et al. 2020; Fattoyev et al. 2020; Lim et al. 2020a; Tews et al. 2021; Rather et al. 2021b; Sedrakian et al. 2020; Beniamini et al. 2020; Biswas et al. 2020; Roupas et al. 2020; Zhou et al. 2021; Wu et al. 2021; Khadkikar et al. 2021; Bombaci et al. 2020; Goncalves & Lazzari 2020; Christian & Schaffner-Bielich 2021; Demircik et al. 2021; Li et al. 2020; Riahi & Kalantari 2021; Dhiman et al. 2007; Shahrbaf et al. 2020; Thapa & Sinha 2020; Huang et al. 2020b; Lim et al. 2020b; Tan et al. 2020; Gupta et al. 2020; Dexheimer et al. 2021).

Different values of NS radii have been obtained from the analysis of X-ray spectra emitted by NSs (Özel et al. 2010; Lattimer & Steiner 2014; Lattimer & Prakash 2016; Özel & Freire 2016). Lattimer & Prakash determined the range for radius at the NS canonical mass $10.7 \leq R_{1.4} \leq 13.1$ km from the properties of symmetric matter and nuclear experiments (Lattimer & Prakash 2016). The recent measurement of the radius for the NS canonical mass inferred from PSR J0030+0451 by the Neutron Star Interior Composition Explorer (NICER) (Gendreau et al. 2016) is $R = 13.02^{+1.24}_{-1.06}$ km for $M = 1.44^{+0.15}_{-0.14} M_{\odot}$ (Miller et al. 2019) or

$R = 12.71^{+1.14}_{-1.19}$ km for $M = 1.34^{+0.15}_{-0.16} M_{\odot}$ (Riley *et al.* 2019), obtained using a Bayesian inference approach. In Ref. (Fattoyev *et al.* 2018), an upper limit on the NS radius for $1.4 M_{\odot}$, $R_{1.4} \leq 13.76$ km was deduced. The measurements from NICER provide an estimate of the canonical mass NS radius within a precision of 1 km. For a canonical mass NS with small radius, a softening of the pressure of neutron matter at intermediate density is required, which results in a small value of the nuclear symmetry energy around saturation density ρ_0 (Lattimer & Prakash 2007; Özel & Freire 2016). However, the requirement of the $2M_{\odot}$ NS doesn't allow the pressure to be reduced too much. The small radius and large mass constraints are satisfied simultaneously by very few models that provide an additional accurate description of finite nuclei properties (Chen & Piekarewicz 2015; Jiang *et al.* 2015; Guichon *et al.* 2018).

At densities of a few times normal nuclear density, the composition of matter inside NS is not known. With increasing density, the appearance of exotic degrees of freedom inside NSs is possible and has been studied over the past decade. In particular, the appearance of hyperonic matter under NS inner core conditions is energetically favored (Ambartsumyan & Saakyan 1960; Glendenning 1985). The onset of hyperons reduces the pressure, leading to a softer EoS as they open new channels filling their Fermi sea, which decreases the maximum mass of NSs by about $0.5 M_{\odot}$ (Glendenning 1982; Chatterjee & Vidaña 2016). Several works has been performed recently considering hyperonic matter in NSs (Li & Sedrakian 2019a; Li *et al.* 2018b; Li & Sedrakian 2019b; Sedrakian *et al.* 2020; Fortin *et al.* 2017; Li *et al.* 2018a; Baldo *et al.* 2000; Tolos *et al.* 2017; Colucci & Sedrakian 2014; Gusakov *et al.* 2014; Bhowmick *et al.* 2014; Oertel *et al.* 2015; Chatterjee & Vidaña 2016; Lopes & Menezes 2018; Isaka *et al.* 2017; Spinella & Weber 2019; Guichon *et al.* 2018; Vidaña 2018; Fortin *et al.* 2020; Tolos & Fabbietti 2020; Gomes *et al.* 2015; Dexheimer & Schramm 2008; Fortin *et al.* 2021).

Heavy NSs are expected to contain exotic matter in their interior, even if they are rotating fast (Avancini *et al.* 2018; Dexheimer *et al.* 2021). Very massive and/or fast rotating stars could be the result of accretion, or even a previous stellar merger, both of which have been shown to enhance stellar magnetic fields (Pons & Viganò 2019; Bransgrove *et al.* 2017; Yakhshiev *et al.* 2019; Aguirre 2020; Zhong & Dai 2020; Most *et al.* 2019; Ciolfi *et al.* 2019; Giacomazzo *et al.* 2015; Xue *et al.* 2019; Raynaud *et al.* 2020; Sur & Haskell 2021). With exceptionally high density, a magnetic field reaching $\approx 10^9$ to 10^{18} G (Bocquet *et al.* 1995; Cardall *et al.* 2001; Chatterjee *et al.* 2015) is attainable in massive NS centers. Among various classes of compact stars available, Anomalous X-ray pulsars (AXPs) and the Soft gamma repeaters (SGRs), usually called magnetars (Mereghetti *et al.* 2015; Kaspi & Beloborodov 2017), are considered to have surface magnetic field within the order 10^{14} - 10^{15} G (Harding & Lai 2006; Turolla *et al.* 2015). Fast radio bursts (FRBs) have also shown evidence of magnetars (Margalit *et al.* 2020; Beniamini *et al.* 2020; Beloborodov 2020; Levin *et al.* 2020; Zanazzi & Lai 2020). Previous works have studied the effect of the magnetic field on the NS Equation of state (EoS) and on the stellar properties like mass and radius (Chakrabarty *et al.* 1997; Broderick *et al.* 2000; Rabhi *et al.* 2008b; Mallick & Schramm 2014; Bandyopadhyay *et al.* 1997; Aguirre 2019; Gomes *et al.* 2017; Dexheimer *et al.* 2012; Pili *et al.* 2017; Felipe *et al.* 2008; Paulucci *et al.* 2013; Casali *et al.* 2014; Rabhi *et al.* 2008a). The presence of strong magnetic fields deviates neutron-star structures from spherical symmetry very strongly and, hence, the spherically symmetric Tolman–Oppenheimer–Volkoff (TOV) equations can no longer be applied for studying their macroscopic structure (Chatterjee *et al.* 2015; Gomes *et al.* 2019).

In the present work, we employ recently proposed density-dependent Relativistic Mean-Field (DD-RMF) parameter sets to study the properties of NSs. By reproducing different hyperon–hyperon optical potentials, the values of the hyperon couplings are obtained, using several different coupling schemes, which are then used to model hyperons in our calculations. The presence of hyperons lowers NS maximum masses (to a value still larger than $2 M_{\odot}$) by softening the EoS, although the radius at the NS canonical mass remains insensitive to them. We further analyze the effect of magnetic fields on nucleonic and hyperonic matter by employing a realistic chemical potential-dependent magnetic field (Dexheimer *et al.* 2017). The macroscopic stellar matter properties for the magnetic EoSs are obtained using the publicly available Language Objet pour la RElativité NumériquE (LORENE) library (LORENE -; Bocquet *et al.* 1995; Bonazzola *et al.* 1993), which solves the coupled Einstein–Maxwell field equations in order to determine stable magnetic star configurations. In this case, NSs become more massive, especially the ones containing hyperons in their interior.

The paper is organized as follows: in section 2, the density-dependent RMF model is presented and the inclusion of the magnetic field for the beta-equilibrium EoS is discussed. The various DD-RMF parameter sets, nuclear matter properties, and hyperon couplings are discussed in section 3. The nucleonic and hyperonic EoSs are described in subsection 4.1, along with spherical solutions for star matter properties. Subsection 4.2 deals with the neutron and hyperon EoS with effects of magnetic fields, together with the discussion of their stellar properties. Subsection 4.3 presents additional results produced assuming different hyperon couplings. We summarize our results and outline an outlook for the future in sec. 5. Finally, the equations of motion and the expressions for the energy and baryon density in the presence of magnetic fields are shown in Appendix A.

2. Theory and Formalism

The Lagrangian density is usually the starting point in RMF theory: the baryons interact through meson exchanges, including the scalar-isoscalar sigma σ , the vector-isoscalar ω , and the vector-isovector ρ . The Lagrangian density contains contributions from the baryonic octet, leptons and the mesons, followed by the interactions between them. Within the DD-RMF model, the coupling constants are density-dependent (Brockmann & Toki 1992), as shown in the following.

The DD-RMF Lagrangian density is written as (Huang *et al.* 2020a)

$$\begin{aligned} \mathcal{L}_m = \sum_B \bar{\psi}_B & \left\{ \gamma_\mu \left(iD^\mu - g_\omega(\rho_B) \omega_\mu - \frac{1}{2} g_\rho(\rho_B) \rho_\mu \tau \right) \right. \\ & \left. - \left(M - g_\sigma(\rho_B) \sigma \right) \right\} \psi_B + \frac{1}{2} \left(\partial^\mu \sigma \partial_\mu \sigma - m_\sigma^2 \sigma^2 \right) \\ & - \frac{1}{4} W^{\mu\nu} W_{\mu\nu} + \frac{1}{2} m_\omega^2 \omega_\mu \omega^\mu - \frac{1}{4} R^{\mu\nu} R_{\mu\nu} + \frac{1}{2} m_\rho^2 \rho_\mu \rho^\mu \\ & + \sum_l \bar{\psi}_l (i\gamma_\mu D^\mu - m_l) \psi_l, \end{aligned} \quad (1)$$

where B sums over the baryon octet ($n, p, \Lambda, \Sigma^+, \Sigma^0, \Xi^0, \Xi^-$) and l over e^- and μ^- . ψ_B and ψ_l represent the baryonic and leptonic Dirac fields, respectively. The mesonic tensor fields and

covariant derivative are defined as

$$\begin{aligned} W^{\mu\nu} &= \partial^\mu W^\nu - \partial^\nu W^\mu, \\ R^{\mu\nu} &= \partial^\mu R^\nu - \partial^\nu R^\mu, \\ D^\mu &= \partial^\mu + eQA^\mu. \end{aligned} \quad (2)$$

The Lagrangian density for the pure electromagnetic part is written as

$$\mathcal{L}_f = -\frac{1}{16\pi} F_{\mu\nu} F^{\mu\nu}, \quad (3)$$

where, $F_{\mu\nu}$ is the electromagnetic field tensor, $F_{\mu\nu} = \partial_\mu A_\nu - \partial_\nu A_\mu$. Hence, the total Lagrangian density in the presence of a magnetic field is

$$\mathcal{L} = \mathcal{L}_m + \mathcal{L}_f. \quad (4)$$

The density dependent coupling constants in the DD-RMF model are parametrized by the relation

$$g_{iB}(\rho_B) = g_{iB}(\rho_0) f_i(x), \quad (5)$$

for $i = \sigma, \omega$. The function $f_i(x)$, where $x = \rho_B/\rho_0$ with ρ_0 as the nuclear matter saturation density, is defined as

$$f_i(x) = a_i \frac{1 + b_i(x + d_i)^2}{1 + c_i(x + d_i)^2}. \quad (6)$$

For the ρ meson, the density-dependent coupling constant is given by an exponential relation as

$$g_\rho(\rho_B) = g_\rho(\rho_0) \exp[-a_\rho(x - 1)]. \quad (7)$$

This parametrization has eight parameters, which are reduced to three using the constraint conditions from refs (Typel & Wolter 1999; Rather et al. 2021b) to reproduce symmetric and asymmetric nuclear matter properties.

For the present case that includes all baryons from the octet, the NS chemical equilibrium condition between different particles are

$$\begin{aligned} \mu_n &= \mu_{\Sigma^0} = \mu_{\Xi^0}, \\ \mu_p &= \mu_{\Sigma^+} = \mu_n - \mu_e, \\ \mu_{\Sigma^-} &= \mu_{\Xi^-} = \mu_n + \mu_e, \\ \mu_\mu &= \mu_e. \end{aligned} \quad (8)$$

The charge neutrality condition follows as

$$\rho_p + \rho_{\Sigma^+} = \rho_e + \rho_{\mu^-} + \rho_{\Sigma^-} + \rho_{\Xi^-}. \quad (9)$$

The expressions for the energy density and pressure in presence of a magnetic field can be obtained by solving the energy-momentum tensor relation

$$T^{\mu\nu} = T_m^{\mu\nu} + T_l^{\mu\nu}, \quad (10)$$

where (Huang et al. 2010; Khalilov 2002)

$$\begin{aligned} T_m^{\mu\nu} &= \mathcal{E}_m u^\mu u^\nu - P(g^{\mu\nu} - u^\mu u^\nu) \\ &+ \mathcal{M}B\left(g^{\mu\nu} - u^\mu u^\nu + \frac{B^\mu B^\nu}{B^2}\right), \\ T_l^{\mu\nu} &= \frac{B^2}{4\pi}\left(u^\mu u^\nu - \frac{1}{2}g^{\mu\nu}\right) - \frac{B^\mu B^\nu}{4\pi}. \end{aligned} \quad (11)$$

Here, \mathcal{M} is the magnetization per unit volume and $B^\mu B_\mu = -B^2$. For the nuclear matter in presence of a magnetic field, the single

particle energy of all charged baryons and leptons is quantized in the direction perpendicular to the magnetic field.

For a uniform magnetic field locally pointing in the z -direction, $B = B\hat{z}$, the total energy of a charged particle becomes

$$E_{cb} = \sqrt{k_z^2 + M^{*2} + 2\nu|q|B}, \quad (12)$$

The quantity $\nu = (n + \frac{1}{2} - \frac{1}{2}\frac{q}{|q|}\sigma_z) = 0, 1, 2, \dots$ indicates the Landau levels of fermions with electric charge q . n is the orbital angular momentum quantum number and σ_z is the Pauli matrix. The Fermi momentum of all baryons charged $k_{F,v}^{cb}$ and leptons $k_{F,v}^l$ with Fermi energies E_F^{cb} and E_F^l , respectively, are given as (Broderick et al. 2000)

$$\begin{aligned} k_{F,v}^{cb} &= \sqrt{(E_F^{cb})^2 - M_{cb}^{*2} - 2\nu|q_{cb}|B}, \\ k_{F,v}^l &= \sqrt{(E_F^l)^2 - m_l^2 - 2\nu|q_l|B}. \end{aligned} \quad (13)$$

The highest value of ν is obtained with sum over Landau levels under the condition that the Fermi momentum of each particle is positive

$$\begin{aligned} \nu_{max} &= \left[\frac{(E_F^{cb})^2 - M_{cb}^{*2}}{2|q_{cb}|B} \right], \\ \nu_{max} &= \left[\frac{(E_F^l)^2 - m_l^2}{2|q_l|B} \right], \end{aligned} \quad (14)$$

for charged baryons cb and leptons, respectively.

The expressions for the matter energy density and baryon density obtained in presence of magnetic field are shown in Appendix A. From Eq. 11, the total energy density is

$$\mathcal{E} = \mathcal{E}_m + \frac{B^2}{8\pi}. \quad (15)$$

The total pressure in the perpendicular and the parallel directions to the local magnetic field are

$$\begin{aligned} P_\perp &= P_m - \mathcal{M}B + \frac{B^2}{8\pi}, \\ P_\parallel &= P_m - \frac{B^2}{8\pi}, \end{aligned} \quad (16)$$

where the magnetization is calculated as

$$\mathcal{M} = \partial P_m / \partial B. \quad (17)$$

3. Parameter Sets

For the present study, we employ two recently proposed density dependent DD-MEX (Taninah et al. 2020), and DD-LZ1 (Wei et al. 2020) parameter sets. These include the necessary tensor couplings of the vector mesons to nucleons and were obtained by fitting the ground state properties of finite nuclei, which considered parametric corrections and shell evaluations of mesons. Additionally, widely used parameter sets DD-ME1 (Nikšić et al. 2002) and DD-ME2 (Lalazissis et al. 2005) are also used. Table 1 displays the nucleon and meson masses and the coupling constants between nucleon and mesons for the given parameter sets. The parameters a, b, c, d for σ, ω , and ρ mesons are also shown.

Some important nuclear matter properties for the DD-LZ1, DD-ME1, DD-ME2, and DD-MEX parameter sets are also shown

Table 1. Nucleon and meson masses and different coupling constants for various DD-RMF parameter sets. Nuclear matter properties: density, binding energy (E/A), incompressibility (K_0), symmetry energy (J), slope parameter (L), and nucleon effective masses at saturation density are also shown.

	DD-LZ1	DD-ME1	DD-ME2	DD-MEX
m_n	938.9000	939.0000	939.0000	939.0000
m_p	938.9000	939.0000	939.0000	939.0000
m_σ	538.6192	549.5255	550.1238	547.3327
m_ω	783.0000	783.0000	783.0000	783.0000
m_ρ	769.0000	763.0000	763.0000	763.0000
$g_\sigma(\rho_0)$	12.0014	10.4434	10.5396	10.7067
$g_\omega(\rho_0)$	14.2925	12.8939	13.0189	13.3388
$g_\rho(\rho_0)$	15.1509	7.6106	7.3672	7.2380
a_σ	1.0627	1.3854	1.3881	1.3970
b_σ	1.7636	0.9781	1.0943	1.3350
c_σ	2.3089	1.5342	1.7057	2.0671
d_σ	0.3799	0.4661	0.4421	0.4016
a_ω	1.0592	1.3879	1.3892	1.3926
b_ω	0.4183	0.8525	0.9240	1.0191
c_ω	0.5386	1.3566	1.4620	1.6060
d_ω	0.7866	0.4957	0.4775	0.4556
a_ρ	0.7761	0.5008	0.5647	0.6202
$\rho_0(fm^{-3})$	0.158	0.152	0.152	0.152
$E/A(MeV)$	-16.126	-16.668	-16.233	-16.140
$K_0(MeV)$	231.237	243.881	251.306	267.059
$J(MeV)$	32.016	33.060	32.310	32.269
$L(MeV)$	42.467	55.428	51.265	49.692
M_n^*/M	0.558	0.578	0.572	0.556
M_p^*/M	0.558	0.578	0.572	0.556

in table (1). The symmetry energy parameter J for the listed parameter sets is compatible with the values $J = 31.6 \pm 2.66$ MeV (Li & Han 2013). The symmetry energy slope parameter L also satisfies recent constraints $L = 59.57 \pm 10.06$ MeV (Zhang et al. 2020; Danielewicz & Lee 2014). The currently accepted value of incompressibility determined from the isoscalar giant monopole resonance (ISGMR) lies in the range $K_0 = 240 \pm 20$ MeV. The K_0 value for all the given parameter sets is within this range, except for the DD-MEX, which predicts a value little higher.

The density-dependent coupling constants of the hyperons to the vector mesons are determined from the SU(6) symmetry as (Banik & Bandyopadhyay 2001; Schaffner & Mishustin 1996; Banik et al. 2014; Tolos et al. 2016)

$$\begin{aligned} \frac{1}{2}g_{\omega\Lambda} &= \frac{1}{2}g_{\omega\Sigma} = g_{\omega\Xi} = \frac{1}{3}g_{\omega N}, \\ \frac{1}{2}g_{\rho\Sigma} &= g_{\rho\Xi} = g_{\rho N}, g_{\rho\Lambda} = 0. \end{aligned} \quad (18)$$

These couplings are calculated by fitting the hyperon optical potential obtained from the experimental data. See Refs. (Inoue 2019a,b) for current lattice calculations and experimental data for these potentials.

The hyperon coupling to the σ field is obtained, so as to reproduce the hyperon potential in symmetric nuclear matter (SNM) derived from the hypernuclear observables (Banik et al.

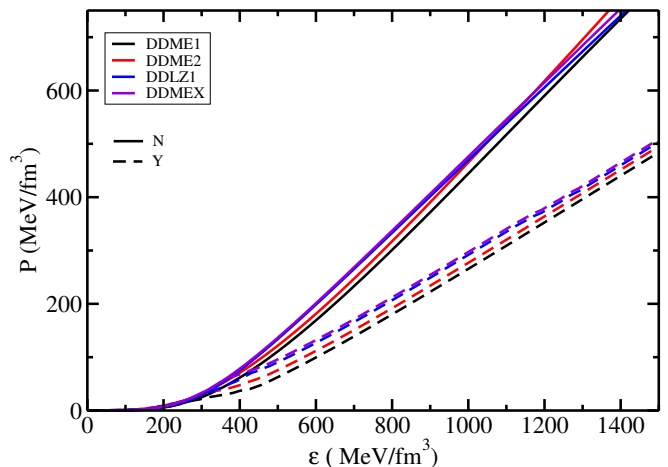


Fig. 1. (color online) Dense matter Equation of State for the DD-LZ1, DD-ME1, DD-ME2, and DD-MEX parameter sets. The solid lines represent pure nucleonic matter, while the dashed lines represent hyperonic matter including the entire baryon octet.

2014; Klevansky 1992)

$$U_\Lambda^N(\rho) = g_{\omega\Lambda}\omega_0 + \sum_R -g_{\sigma\Lambda}\sigma_0. \quad (19)$$

For the present study, we reproduce the following optical potentials for the hyperons (Thapa et al. 2020)

$$\begin{aligned} U_\Lambda^N(\rho_0) &= -30 \text{ MeV}, \\ U_\Sigma^N(\rho_0) &= +30 \text{ MeV}, \\ U_\Xi^N(\rho_0) &= -14 \text{ MeV}. \end{aligned} \quad (20)$$

These potentials correspond to the value of the density-dependent scalar couplings $g_{\sigma\Lambda}/g_{\sigma N} = 0.6105$, $g_{\sigma\Sigma}/g_{\sigma N} = 0.3024$, and $g_{\sigma\Xi}/g_{\sigma N} = 0.4426$.

4. Results and Discussions

4.1. Nucleonic and Hyperonic neutron stars

The EoS of pure nucleonic (solid lines) and hyperonic matter (dashed lines) under chemical-equilibrium and charge neutrality conditions for several DD-RMF parameter sets are displayed in figure 1. For pure nucleonic matter, the DD-MEX parameter set produces a stiff EoS at low density region, while the DD-ME2 set produces a stiff EoS in the high density regime. The hyperons start to appear in the density range ≈ 300 -400 MeV/fm 3 for all parameter sets. The onset of hyperonization softens the EoS (reduction in the pressure) due to the hyperons replacing the neutrons and opening new channels to distribute the Fermi energy. To build a unified EoS, the Baym-Pethick-Sutherland (BPS) EoS (Baym et al. 1971) has been used in the outer crust region. For the inner crust part, the EoS for non-uniform matter is generated by using DD-ME2 parameter set in a Thomas-Fermi approximation (Avancini et al. 2009; Pais & Providência 2016; Rather et al. 2021a). All the DD-RMF parameter sets considered are very similar in the outer crust density regime.

With the EoSs obtained for pure nucleonic and hyperonic matter, stellar matter properties like mass and radius are obtained by solving the Tolmann-Oppenheimer-Volkov (TOV) coupled differential equations (Tolman 1939; Oppenheimer & Volkoff 1939) for a static isotropic spherically symmetric star

$$\frac{dP(r)}{dr} = -\frac{[\mathcal{E}(r) + P(r)][M(r) + 4\pi r^3 P(r)]}{r^2(1 - 2M(r)/r)}, \quad (21)$$

and

$$\frac{dM(r)}{dr} = 4\pi r^2 \mathcal{E}(r), \quad (22)$$

where $M(r)$ contained in the radius r represents the gravitational mass for a specific EoS and a given choice of central energy density \mathcal{E}_c .

The tidal deformability λ is defined as (Hinderer et al. 2010; Kumar et al. 2017)

$$\lambda = -\frac{Q_{ij}}{\mathcal{E}_{ij}} = \frac{2}{3} k_2 R^5, \quad (23)$$

where, Q_{ij} represents the mass quadrupole moment of a star and \mathcal{E}_{ij} corresponds to its external tidal field. The dimensionless tidal deformability Λ is related to the compactness parameter $C = M/R$ as

$$\Lambda = \frac{\lambda}{M^5} = \frac{2k_2}{3C^5}, \quad (24)$$

where k_2 is the second love number. To estimate the love number along with the evaluation of the TOV equations, the function $y = y(R)$ as defined in ref (Hinderer 2008) is computed with the initial condition of $y(0) = 2$ for the second love number. This value can be computed from the following first-order differential equations (Kumar et al. 2017; Hinderer 2008)

$$r \frac{dy(r)}{dr} + y(r)^2 + y(r)F(r) + r^2 Q(r) = 0, \quad (25)$$

where,

$$F(r) = \frac{r - 4\pi r^3 [\mathcal{E}(r) - P(r)]}{r - 2M(r)}, \quad (26)$$

$$Q(r) = \frac{4\pi r (5\mathcal{E}(r) + 9P(r) + \frac{\mathcal{E}(r) + P(r)}{\partial P(r)/\partial \mathcal{E}(r)} - \frac{6}{4\pi r^2})}{r - 2M(r)} - 4 \left[\frac{M(r) + 4\pi r^3 P(r)}{r^2 (1 - 2M(r)/r)} \right]^2. \quad (27)$$

Once the above equations are solved for $y = y(R)$ with R being the radius of the spherical star in isolation, the second tidal love number is obtained from the following expression (Hinderer et al. 2010)

$$k_2 = \frac{8}{5} (1 - 2C)^2 [2C(y - 1)] \{ 2C(4(y + 1)C^4 + (6y - 4)C^3 + (26 - 22y)C^2 + 3(5y - 8)C - 3y + 6) - 3(1 - 2C)^2 (2C(y - 1) - y + 2) \log \left(\frac{1}{1 - 2C} \right) \}^{-1}. \quad (28)$$

Given the initial boundary conditions for the NS at the center $P(0) = P_c$, $M(0) = 0$, and $y(0) = 2$ with P_c as the central pressure, to the surface of the star $P(R) = 0$, $M(R) = M$, and $r(R) = R$, the above equations are solved for a given central density to determine the macroscopic properties of a NS.

Figure 2 shows the mass-radius relation for pure nucleonic and hyperonic matter for the parameter sets DD-ME1, DD-ME2, DD-LZ1, and DD-MEX. The shaded areas represent the recent constraints on the NS maximum mass inferred from GW190814 ($M=2.50\pm 2.67 M_\odot$), the massive pulsars MSP J0740+6620 ($M=2.14^{+0.10}_{-0.09} M_\odot$), and PSR J0348+0432 ($M=2.01\pm 0.04 M_\odot$).

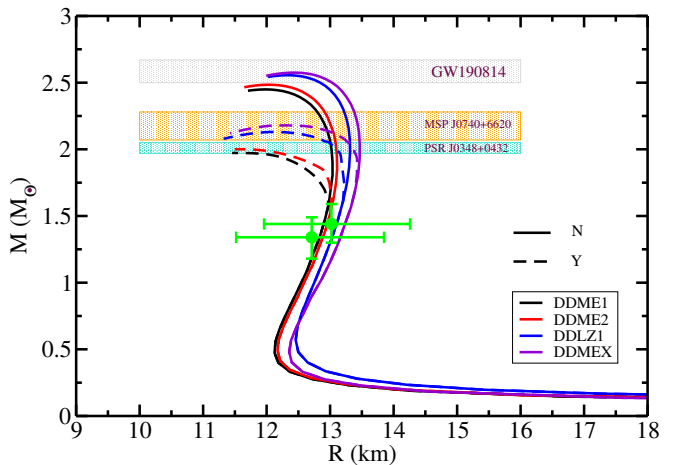


Fig. 2. (color online) Mass-Radius relation for pure nucleonic (solid lines) and hyperonic (dashed lines) stars using several DD-RMF parameter sets. The colored areas show recent constraints inferred from GW190814 and from the massive pulsars MSP J0740+6620 and PSR J0348+0432 (Abbott et al. 2020; Cromartie & Fonseca et al. 2019; Antoniadis & Freire et al. 2013). The constraints on the mass-radius limits inferred from NICER observations (Miller et al. 2019; Riley et al. 2019) are also shown.

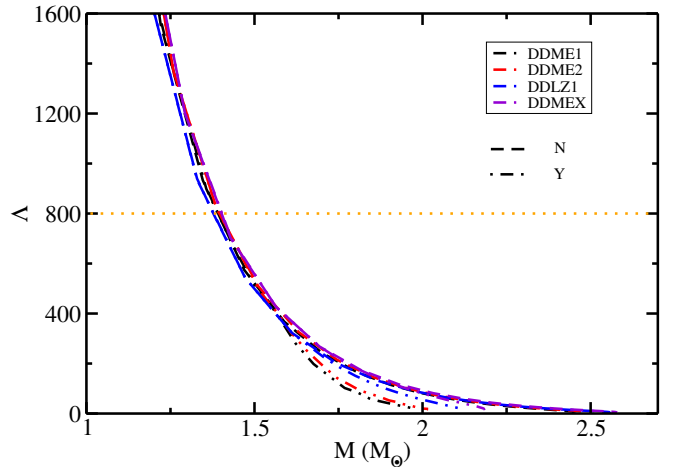


Fig. 3. (color online) Dimensionless tidal deformability variation with the NS mass for nucleonic (dashed lines) and hyperonic (dot dashed lines) stars using DD-LZ1, DD-ME1, DD-ME2, and DD-MEX parameter sets. The orange dotted line represents the upper limit on the dimensionless tidal deformability set by measurement from GW170817 (Abbott et al. 2017).

The constraints on the radius limits around the NS canonical mass inferred from PSR J0030+0451 by NICER, $R=13.02^{+1.24}_{-1.06}$ km at $M=1.44^{+0.15}_{-0.14} M_\odot$ (Miller et al. 2019) and $R=12.71^{+1.14}_{-1.19}$ km at $M=1.34^{+0.15}_{-0.16} M_\odot$ (Riley et al. 2019), are also shown. For pure nucleonic matter, the DD-LZ1 and DD-MEX parameter sets reach a maximum mass of 2.55 and $2.57 M_\odot$, with a radius of 12.30 and 12.46 km, respectively, indicating the possibility of GW190814 secondary component being a very massive NS. The hyperonic counterparts of the given DD-RMF parameter sets, which soften the EoS, produce a maximum mass of 2.18 and $2.13 M_\odot$ with a radius of 12.24 and 12.07 km respectively. For the DD-ME1 and DD-ME2 parameter sets, the NS maximum mass decreases from 2.45 and 2.48 to 1.98 and $2.01 M_\odot$ respectively, while the respective radius decreases by ≈ 0.5 km. The radius at the NS canonical mass, $R_{1.4}$, remains insensitive to the appearance of

Table 2. Properties of pure nucleonic and hyperonic NSs for different DD-RMF parameter sets, including maximum mass, respective radius, and radius and dimensionless tidal deformability of a $1.4 M_{\odot}$ star.

	Nucleonic star				Hyperonic star			
	M_{max} (M_{\odot})	R (km)	$R_{1.4}$ (km)	$\Lambda_{1.4}$	M_{max} (M_{\odot})	R (km)	$R_{1.4}$ (km)	$\Lambda_{1.4}$
DD-ME1	2.449	11.981	12.898	689.342	1.983	11.515	12.898	689.342
DD-ME2	2.483	12.017	12.973	733.149	2.013	11.674	12.973	733.149
DD-LZ1	2.555	12.297	13.069	728.351	2.130	12.067	13.069	728.351
DD-MEX	2.575	12.465	13.168	791.483	2.183	12.238	13.168	791.483

hyperons. The hyperonic configurations satisfy the maximum mass limit from the massive pulsars MSP J0740+6620 and PSR J0348+0432, but are inconsistent with the GW190814 potential constraint (see discussion in Sedrakian et al. (2020)). All of the nucleonic and hyperonic configurations satisfy the mass-radius limits inferred from NICER.

The variation of the dimensionless tidal deformability with the NS mass for the nucleonic and hyperonic stars based on the DD-RMF parametrizations are shown in figure 3. The dimensionless tidal deformability of pure nucleonic as well as hyperonic matter for all the parameter sets lies well below the upper limit of $\Lambda_{1.4}=800$ obtained from the gravitational wave event GW170817 (Abbott et al. 2017). The shift in the tidal deformability for the hyperonic matter is seen as the mass increases. Table 2 displays the different properties of neutron and hyperonic stars obtained with different DD-RMF parameter sets.

4.2. Magnetic stars

In order to study the effects of magnetic fields on our microscopic description of matter, we employ a chemical potential-dependent magnetic field derived from the solutions of the Einstein-Maxwell's equations. The quadratic relation between the magnetic field and the chemical potential depends on the magnetic dipole moment and is given by (Dexheimer et al. 2017)

$$B^*(\mu_B) = \frac{(a + b\mu_B + c\mu_B^2)}{B_c^2} \mu, \quad (29)$$

with μ_B being the baryon chemical potential in MeV and μ the dipole magnetic moment in units of Am^2 to produce B^* in units of the electron critical field $B_c = 4.414 \times 10^{13} \text{ G}$. The coefficients a , b , and c taken as $a = -0.0769 \text{ G}^2/(\text{Am}^2)$, $b = 1.20 \times 10^{-3} \text{ G}^2/(\text{Am}^2 \text{ MeV})$ and $c = -3.46 \times 10^{-7} \text{ G}^2/(\text{Am}^2 \text{ MeV}^2)$ are obtained from a fit for the magnetic field in the polar direction of a star with a baryon mass of $2.2 M_{\odot}$.

Figure 4 displays the magnetic field profile as a function of baryon density for a $2.2 M_{\odot}$ baryonic mass star obtained for the DD-MEX EoS. The magnetic field effect on the DD-ME2 EoS has already been calculated (Thapa et al. 2020) and the DD-ME1 EoS predicts similar behavior. In Ref. (Thapa et al. 2020), spherically symmetric TOV equations were used for central magnetic fields $\approx 10^{18} \text{ G}$ with a density-dependent and universal profile for magnetic field. Since the DD-MEX EoS predicts a heavier NS than other parameter sets, we choose this parameter set to study magnetic effects and verify whether this model predicts the possibility of the GW190814 secondary component being a hyperonic magnetar. In fig. 4, the dashed curves represent a NS without hyperons and dot-dashed curves represent a NS with hyperons. It is clear that the magnetic field produced by the NS without hyperons is larger. This illustrates that the transition from

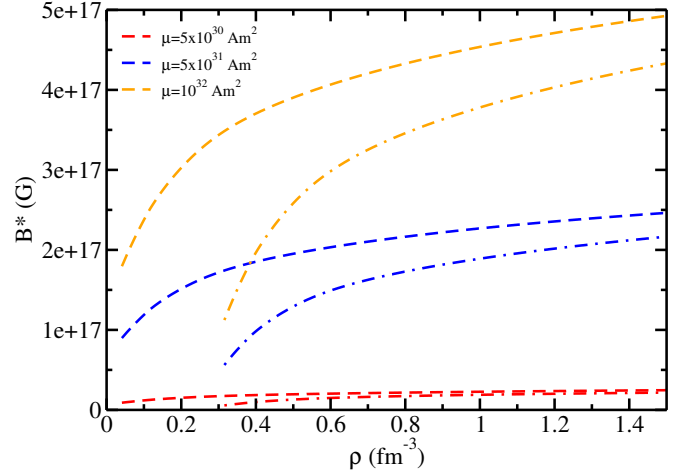


Fig. 4. (color online) Magnetic field profile as a function of baryon density for the DD-MEX EoS with different values of magnetic dipole moment. The dashed lines represent the profile for NS without hyperons, while the dot-dashed lines represent hyperonic stars.

Table 3. Magnetic field at low densities B_s (corresponding to stellar surfaces) and at high values of densities B_c calculated for the DD-MEX EoS with and without hyperons.

μ (Am^2)	Nucleonic star		Hyperonic star	
	B_s (G)	B_c (G)	B_s (G)	B_c (G)
5×10^{30}	1.01×10^{15}	2.59×10^{16}	6.65×10^{15}	1.96×10^{16}
5×10^{31}	8.98×10^{16}	2.28×10^{17}	5.83×10^{16}	1.89×10^{17}
10^{32}	1.79×10^{17}	4.55×10^{17}	1.12×10^{17}	3.77×10^{17}

μ_B to ρ_B is model and particle population dependent. For magnetic dipole moment greater than 10^{31} Am^2 , the magnetic field produced at large densities is larger than 10^{17} G , which is strong enough to cause a large deformation in the NS structure. The values of the magnetic field produced at the surface and at large densities using different values of the magnetic dipole moment for NSs with and without hyperons are shown in table 3. For a magnetic dipole moment 10^{32} Am^2 , the magnetic field produced at large densities is greater than $4 \times 10^{17} \text{ G}$ for both cases.

Figure 5 shows the variation of the transverse pressure vs the energy density for the DD-MEX parameter set with and without hyperons. The solid line represents the variation in the pressure without including magnetic field ($\mu=0$), while the other lines represent the variation obtained with the magnetic field at magnetic dipole moments $\mu=5 \times 10^{30} \text{ Am}^2$, $5 \times 10^{31} \text{ Am}^2$ and 10^{32} Am^2 . The insets show the pressure at higher values of the energy density. It is clear that the change in the pressure at a given value of energy density is larger for a NS with hyperons as compared to the NS

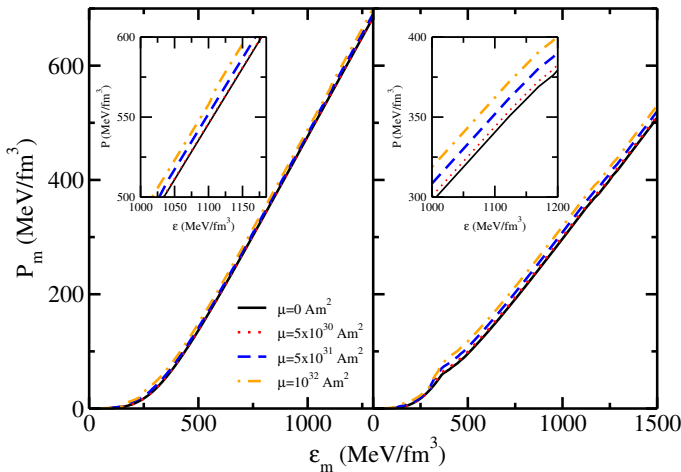


Fig. 5. (color online) Variation of matter pressure in transverse direction vs energy density for the DD-MEX parameter set without and with magnetic field effects at different values of magnetic dipole moment. Left panel depicts the EoSs without hyperons and right panel depicts the EoS with hyperons. The insets in each panel show the variation in the pressure at higher value of the energy density for different magnetic moments.

without hyperons, which implies that the EoS with hyperons becomes stiffer than without hyperons (when compared to the $B=0$ case) in the presence of strong magnetic field. The reason for such behavior will be discussed in the following. The magnetic field produced at the magnetic dipole moment $5 \times 10^{30} \text{ Am}^2$ is of the order of 10^{16} G at the center, which is small enough to be indistinguishable from the zero magnetic case. For higher magnetic dipole moments, the magnetic field produced $\approx 4 \times 10^{17} \text{ G}$ is strong enough to increase the matter pressure to higher values, thus producing a distinguishable effect.

Figure 6 shows the particle fractions as a function of baryon density for beta stable NS matter obtained using the DD-MEX EoS. Figure 6 panel (a) displays the fractions in the absence of magnetic field, while panels (b), (c), and (d) depict the particle fractions in the presence of magnetic fields with fixed magnetic dipole moments $\mu=5 \times 10^{30} \text{ Am}^2$, $\mu=5 \times 10^{31} \text{ Am}^2$, and $\mu=5 \times 10^{32} \text{ Am}^2$, respectively. Clearly, in all the cases, the Λ particle is the dominant hyperonic component, which starts appearing in the density range $2 - 3 \rho_0$ (DHapo et al. 2010; Vidaña 2013; Rather et al. 2018; Sen et al. 2018). The neutral Ξ hyperon appears at a density $\approx 5.5 \rho_0$ for $B=0$, which remains unaltered with the inclusion of the magnetic field. As expected, the charged particles are more strongly affected by the magnetic field and an increase in their population is seen with the increase in the magnetic field strength. For $B=0$ (and all other cases), the e^- and μ^- population is large at low densities, which suppresses the appearance of Ξ^- hyperons. With an increase in the magnetic dipole moment, the magnetic field strength increases, which shifts the appearance of Ξ^- hyperon from ≈ 2.5 to around $\approx 3.5 \rho_0$. At this threshold, the density of the negatively charged leptons e^- and μ^- starts to drop, as the charge neutrality condition from (8) allows the Ξ^- hyperon to take over. Similarly, the appearance of the Λ hyperon accelerates the disappearance of neutrons, as both are neutral particles. Overall, we see that the addition of magnetic field increases the population of leptons (re-leptonizes) and correspondingly decreases the population of hyperons (de-hyperonizes), which renders the EoS stiffer (Tolos et al. 2016).

Because of the repulsive nature of the Σ potential, the formation of Σ^0 and Σ^- is totally suppressed for the densities considered

in the present work. The absence of Σ hyperons is supported by the fact that no bound Σ^- hypernuclei has been found yet, despite several searches (Harada & Hirabayashi 2006, 2015) and this has been reproduced in several works (Glendenning 2001; Thapa et al. 2020; Guichon et al. 2018). The inclusion of strong magnetic fields do not change this feature. The properties of nucleonic and hyperonic stars at different values of the magnetic dipole moment, which correspond to different magnetic field values at the surface and the center, are shown in table 4.

The effect of magnetic field on the mass-radius relation of a NS with and without hyperons is displayed in figure 7. These calculations are performed for the DD-MEX EoS using the LORENE library (LORENE-). Different values of magnetic dipole moment are used to obtain different values of the magnetic field at the stellar surface and at the center. As can be seen, the NS maximum mass without hyperons increases from $2.575 M_\odot$ for $B=0$ to $2.711 M_\odot$ for $\mu=10^{32} \text{ Am}^2$. The corresponding radius changes from 12.465 to 13.474 km . The radius at $1.4 M_\odot$ increases by around 1 km. With the hyperons included, the mass increases from 2.183 to $2.463 M_\odot$ when magnetic field effects are included with $\mu=10^{32} \text{ Am}^2$. The variation obtained in the mass-radius is larger for hyperonic stars than for the pure nucleonic stars due to the additional effect of de-hyperonization that takes place due to the magnetic field. The de-hyperonization results in the enhancement of the matter pressure P_m for a given ϵ_m . For higher magnetic fields produced at magnetic dipole moments $\mu=5 \times 10^{31}$ and $\mu=10^{32} \text{ Am}^2$, the effect of the magnetic field is seen to be very large at smaller stellar masses. For low magnetic fields, pure nucleonic stars still satisfy the possible maximum mass constraint from the GW190814 event, implying the possibility that of its secondary component to be a magnetar. The radius constraints inferred from NICER are satisfied by both nucleonic as well as hyperonic stars with low magnetic fields. For central magnetic fields $\approx 7 \times 10^{16} \text{ G}$, the EoS obtained for pure nucleonic matter satisfies the radius constraints from NICER measurement. For hyperonic matter, a lower magnetic field $\approx 4 \times 10^{16} \text{ G}$ produces a hyperonic star with radius that satisfies NICER constraints. This is due to the fact that for magnetic fields less than 10^{17} G , the deformation produced in the stellar structure is negligible and, hence, the variation in radius is too small when compared to the non-magnetic case. Note that the surface magnetic field of the stars observed by NICER is expected to be $\approx 10^8 \text{ G}$ (Miller et al. 2019).

Figure 8 shows the variation in the dimensionless tidal deformability as a function of gravitational mass with magnetic field effects and considering different values of magnetic dipole moment. The results for EoS with and without hyperons are shown. For pure nucleonic stars, the tidal deformability increases to a value $\Lambda_{1.4} \approx 1500$ for a central magnetic field of $4.55 \times 10^{17} \text{ G}$ produced fixing the magnetic dipole moment to $\mu=10^{32} \text{ Am}^2$, thus violating the constraint on the dimensionless tidal deformability from GW170817, which provides an upper limit of 800 on $\Lambda_{1.4}$ (Abbott et al. 2017). Seen in table 4, a small magnetic field produces a NS with tidal deformability larger than the upper limit from GW170817. This confirms that the BNS merger event GW170817 did not consist of magnetars. For hyperonic stars, the value at $1.4 M_\odot$ remains unchanged when considering a magnetic dipole moment of $\mu=5 \times 10^{30} \text{ Am}^2$. As the magnetic dipole moment increases, stronger magnetic fields increase the stellar radius, which allows the tidal deformability $\Lambda_{1.4}$ to reach a value around 1550. For a nucleonic star and a hyperonic star

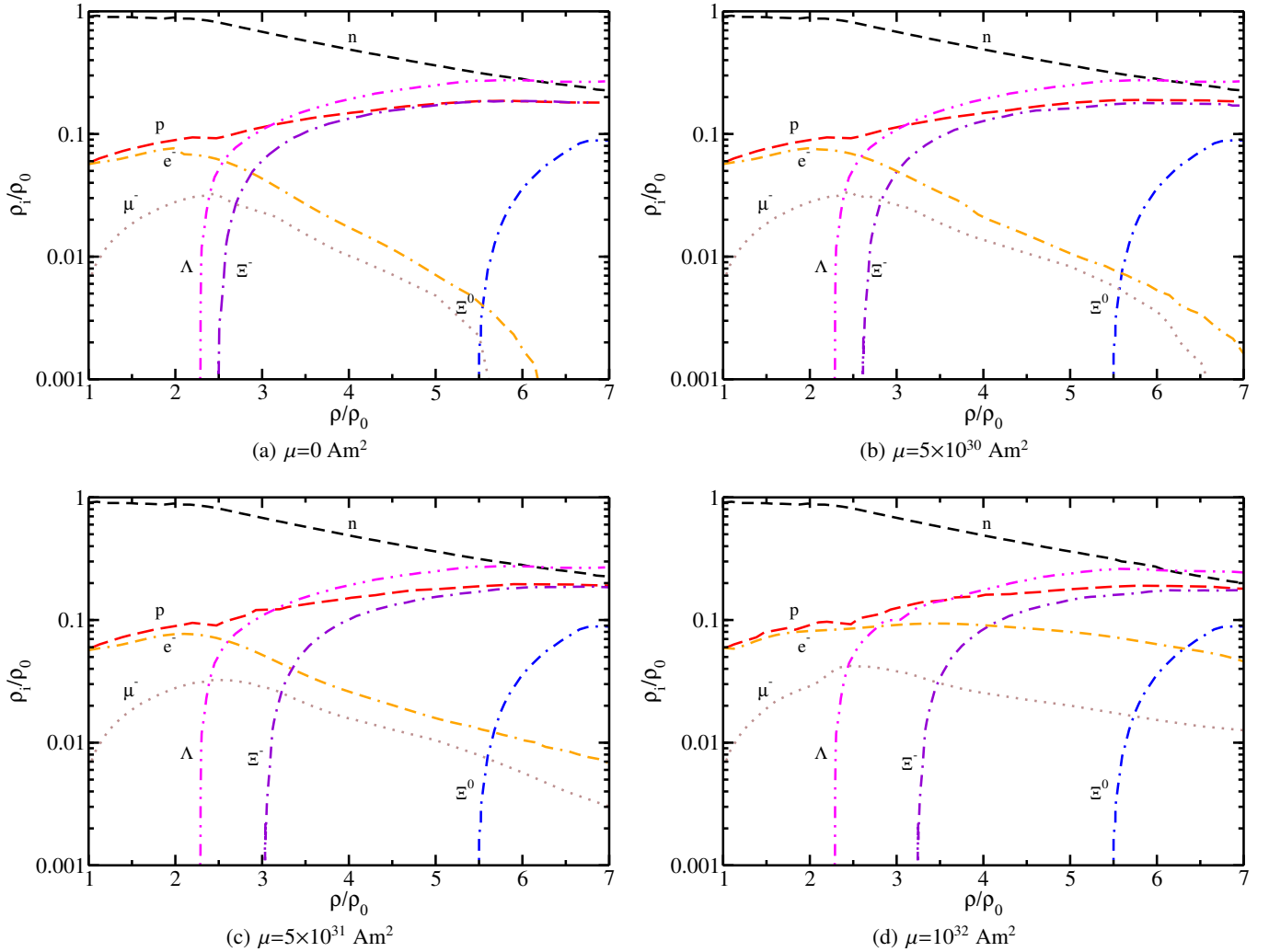


Fig. 6. Particle fraction of the baryons and leptons as a function of normalized baryon density for the DD-MEX model without magnetic field (a) and with magnetic field with different magnetic dipole moments b) $\mu=5 \times 10^{30} \text{ Am}^2$, c) $\mu=5 \times 10^{31} \text{ Am}^2$, and d) $\mu=1 \times 10^{32} \text{ Am}^2$.

Table 4. Stellar properties: Maximum mass (M_{max}), corresponding radius (R_{max}), canonical mass radius ($R_{1.4}$), and dimensionless tidal deformability ($\Lambda_{1.4}$) of pure nucleonic and hyperonic star for the DD-MEX EoS without magnetic field and with magnetic field effects for different values of the magnetic dipole moment.

μ (Am^2)	Nucleonic star				Hyperonic star			
	M_{max} (M_\odot)	R (km)	$R_{1.4}$ (km)	$\Lambda_{1.4}$	M_{max} (M_\odot)	R (km)	$R_{1.4}$ (km)	$\Lambda_{1.4}$
0	2.575	12.465	13.168	791.483	2.183	12.238	13.168	791.483
5×10^{30}	2.580	12.536	13.235	802.801	2.224	12.506	13.168	791.483
5×10^{31}	2.632	13.024	14.507	1175.35	2.325	13.269	14.112	998.882
10^{32}	2.711	13.474	15.027	1517.09	2.463	13.894	15.105	1559.194

with dimensionless tidal deformability well within the limit of GW170817, a magnetic field with a maximum value of $\approx 2 \times 10^{16} \text{ G}$ is required. See Ref (Biswas & Bose 2019) for a discussion of the tidal deformability of deformed stars and Ref. (Zhu et al. 2020) for a discussion on how very large magnetic fields generate new high-order corrections to the deformability that can modify the gravitational-wave evolution of magnetars. Note that magnetic NSs can also be a source of gravitational waves due to their asymmetric nature (Sur & Haskell 2021; Haskell et al. 2008;

Gomes et al. 2019; Bonazzola & Gourgoulhon 1996; Frieben & Rezzolla 2012).

4.3. Additional hyperon couplings

To investigate how different hyperon couplings and hyperon potentials affect the results we presented so far, we use a more general symmetry group SU(3) to determine the coupling constants of all baryons and mesons (Lopes & Menezes 2014, 2021).

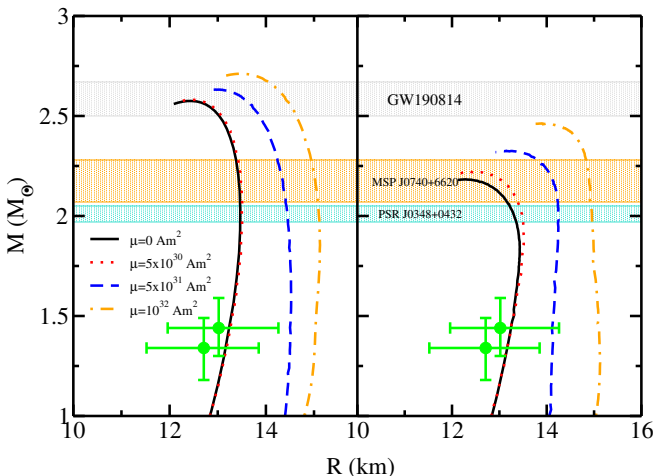


Fig. 7. (color online) Relation between mass and circumferential radius for a NS without magnetic field and with magnetic field effects considering different magnetic dipole moments without hyperons (left panel) and with hyperons (right panel) using the DD-MEX parameter set. The colored areas show the recent constraints inferred from GW190814, MSP J0740+6620, and PSR J0348+0432 (Abbott et al. 2020; Cromartie & Fonseca et al. 2019; Antoniadis & Freire et al. 2013). The constraints on the mass-radius limits inferred from NICER (Miller et al. 2019; Riley et al. 2019) are also shown.

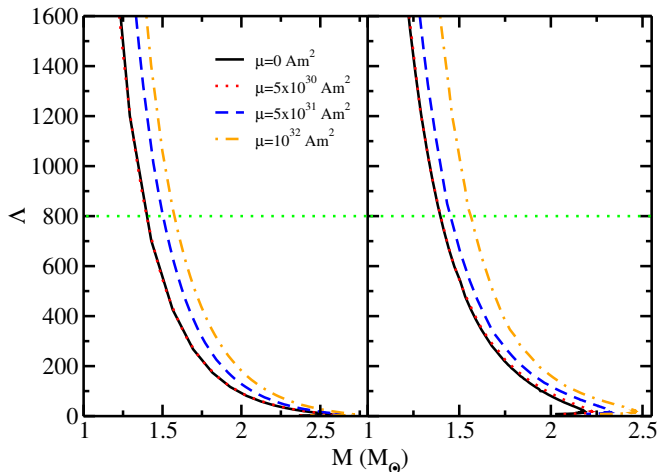


Fig. 8. (color online) Dimensionless tidal deformability (Λ) as a function of NS mass for EoS without magnetic field (solid line) and with magnetic field effects considering different magnetic dipole moments. Left panel shows the results obtained for NS without hyperons, while right panel shows the results for NS with hyperons. The orange dotted line represents the upper limit on the dimensionless tidal deformability set by measurement from GW170817 (Abbott et al. 2017).

For the ω meson, we have

$$\frac{g_{\omega\Lambda}}{g_{\omega N}} = \frac{4 + 2\alpha_v}{5 + 4\alpha_v}, \frac{g_{\omega\Sigma}}{g_{\omega N}} = \frac{8 - 2\alpha_v}{5 + 4\alpha_v}, \frac{g_{\omega\Xi}}{g_{\omega N}} = \frac{5 - 2\alpha_v}{5 + 4\alpha_v}. \quad (30)$$

For the ρ meson, we have

$$\frac{g_{\rho\Sigma}}{g_{\rho N}} = 2\alpha_v, \frac{g_{\rho\Xi}}{g_{\rho N}} = 2\alpha_v - 1, \frac{g_{\rho\Lambda}}{g_{\rho N}} = 0. \quad (31)$$

The hyperon-scalar meson coupling constants are fixed so as to reproduce the following optical potentials (Glendenning & Moszkowski 1991; Dover & Gal 1984; Schaffner et al. 1994;

Table 5. Hyperon meson coupling constants for different values of the hyperon coupling parameter α_v .

	$\alpha_v = 1.0$	$\alpha_v = 0.75$	$\alpha_v = 0.50$	$\alpha_v = 0.25$
$g_{\omega\Lambda}/g_{\omega N}$	0.667	0.687	0.714	0.75
$g_{\omega\Sigma}/g_{\omega N}$	0.667	0.812	1.00	1.25
$g_{\omega\Xi}/g_{\omega N}$	0.333	0.437	0.571	0.75
$g_{\rho\Sigma}/g_{\rho N}$	2.0	1.5	1.0	0.5
$g_{\rho\Xi}/g_{\rho N}$	1.0	0.5	0.0	-0.5
$g_{\sigma\Lambda}/g_{\sigma N}$	0.610	0.626	0.653	0.729
$g_{\sigma\Sigma}/g_{\sigma N}$	0.403	0.514	0.658	0.850
$g_{\sigma\Xi}/g_{\sigma N}$	0.318	0.398	0.500	0.638

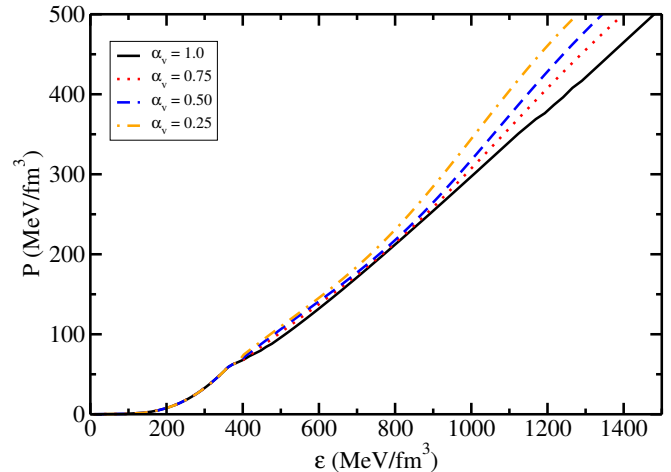


Fig. 9. (color online) EoS for the DD-MEX parameter set at different values of the parameter α_v .

Schaffner-Bielich & Gal 2000)

$$\begin{aligned} U_\Lambda &= -28 \text{ MeV}, \\ U_\Sigma &= +30 \text{ MeV}, \\ U_\Xi &= -18 \text{ MeV}. \end{aligned} \quad (32)$$

The coupling constants at different values of the parameter α_v are displayed in table 5. For $\alpha_v = 1.0$, the hybrid SU(6) group is recovered.

The particle population of hyperons and other particles depend upon the hyperon meson coupling constants, which vary with the parameter α_v . Changing the value of α_v from 1.0 to 0.25 suppresses strange particles. The suppression of Ξ^- increases the lepton fraction at lower value of α_v . The neutrons and protons are the most populated particles at $\alpha_v=0.25$. Figure 9 displays the EoS obtained using different values of the parameter α_v . As the α_v value decreases from 1.0 to 0.25, the stiffness of the EoS increases due to the increase in the value of ω meson couplings.

Figure 10 displays the mass-radius relation for hyperonic stars without magnetic field effects at different values of α_v . Lowering the value of α_v stiffens the EoS, which increases the maximum mass to $2.283 M_\odot$ for $\alpha_v=0.25$ (from $2.183 M_\odot$ for $\alpha_v=1.0$). It is to be mentioned that the stellar properties of hyperonic stars obtained at $\alpha_v = 1.0$ almost resemble to that obtained from the hyperon potentials given by (20). The change in the hyperon potentials alters the values of sigma meson couplings by a small fraction and, hence, the changes obtained in the particle population and stellar properties are negligible.

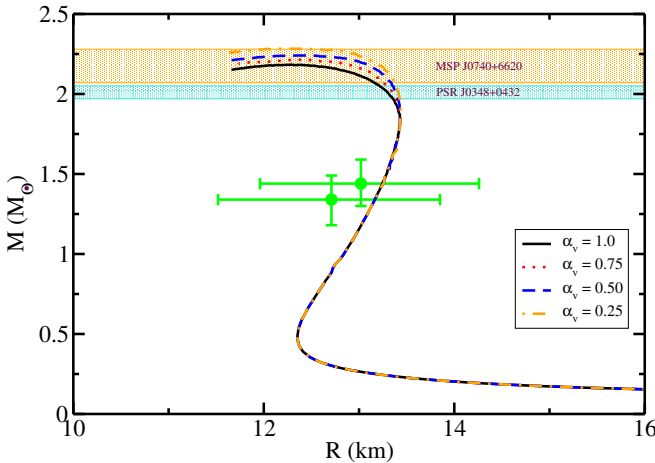


Fig. 10. (color online) Mass-Radius for a NS with hyperons at different values of the parameter α_v using the DD-MEX parameter set. The shaded regions show the recent constraints inferred from GW190814, MSP J0740+6620, and PSR J0348+0432 (Cromartie & Fonseca *et al.* 2019; Antoniadis & Freire *et al.* 2013). The green overlaid arrows show constraints on the mass-radius limits inferred from NICER (Miller *et al.* 2019; Riley *et al.* 2019).

With the addition of magnetic field effects, the results of different hyperon couplings on hyperonic EoSs is determined. Figure 11 displays the relation between mass and radius for a hyperonic star at different α_v values without magnetic field and with magnetic field effects considered at different values of magnetic dipole moment. For $\alpha_v=0.75$, the maximum mass increases to a value $2.437 M_\odot$ for a magnetic dipole moment $\mu=10^{32} \text{ Am}^2$, which corresponds to a central magnetic field of $3.77 \times 10^{17} \text{ G}$. Similarly, for $\alpha_v=0.50$ and 0.25, the maximum mass reaches a value 2.480 and $2.556 M_\odot$, respectively, at $\mu=10^{32} \text{ Am}^2$. This implies that the secondary component of GW190814 could be a hyperonic magnetar. For the present, hyperon couplings with a magnetic dipole moment $\mu=5 \times 10^{31} \text{ Am}^2$, which corresponds to a central magnetic field greater than 10^{17} G , the deviation in the hyperonic star radius at canonical mass is very large, around 1.5 km, as compared to that obtained from previous couplings. But with even stronger magnetic fields, the deviation obtained is less in the present case. This implies that a change in hyperon couplings effects the stellar properties, especially the radius at canonical mass at strong central magnetic field.

Figure 12 displays the variation in the dimensionless tidal deformability of a hyperonic star with magnetic field effects considered at different values of magnetic dipole moment. For small values of the magnetic dipole moment at different values of α_v , the Λ -M curve follows similar pattern as for the previous hyperon couplings. Since the variation in radius at canonical mass are large for the present couplings, the tidal deformability, $\Lambda_{1.4}$ obtained is also large. For $\alpha_v=0.25$, the dimensionless tidal deformability reaches a value of ≈ 1900 for magnetic dipole moment 10^{32} Am^2 . The properties of hyperonic stars using different hyperon coupling values according to the value of α_v with and without magnetic field effects considered at different magnetic dipole moments, are shown in table 6.

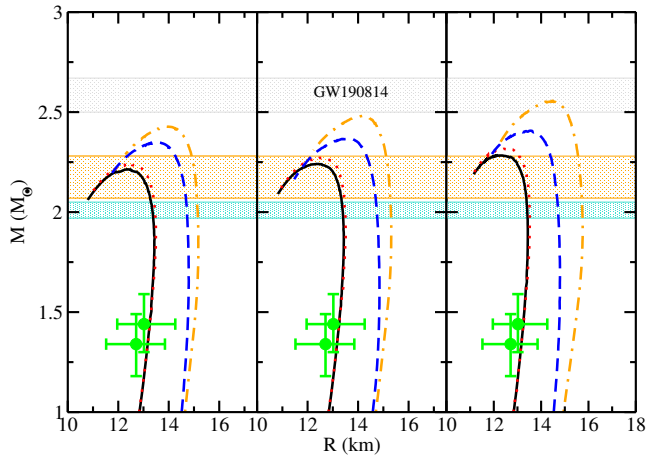


Fig. 11. (color online) Relation between mass and circumferential radius for a hyperonic star with magnetic field effects considering different magnetic dipole moments at different hyperon couplings $\alpha_v=0.75$ (left panel), $\alpha_v=0.50$ (middle panel) and $\alpha_v=0.25$ (right panel) using the DD-MEX parameter set. The colored areas show the recent constraints inferred from GW190814, MSP J0740+6620, and PSR J0348+0432 (Abbott *et al.* 2020; Cromartie & Fonseca *et al.* 2019; Antoniadis & Freire *et al.* 2013). The constraints on the mass-radius limits inferred from NICER (Miller *et al.* 2019; Riley *et al.* 2019) are also shown.

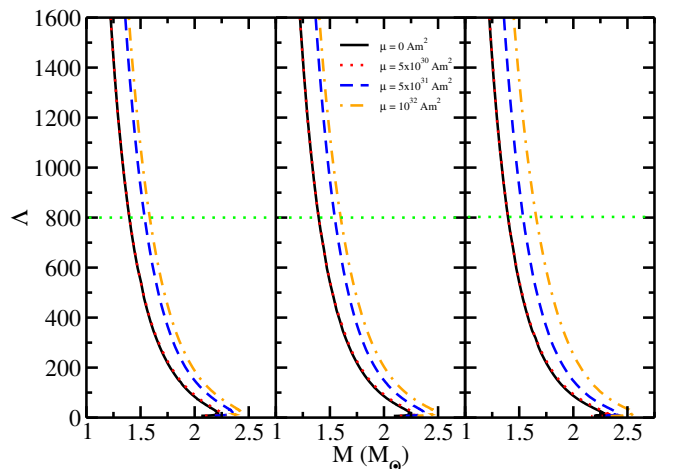


Fig. 12. (color online) Dimensionless tidal deformability as a function of NS mass for EoSs without magnetic field (solid line) and with magnetic field effects considering different magnetic dipole moments. Different panels show the results obtained for hyperonic EoSs at different values of the parameter α_v . The orange dotted line represents the upper limit on the dimensionless tidal deformability set by measurement from GW170817 (Abbott *et al.* 2017).

neutron star (NS) ever detected (in the secondary object of the gravitational wave event GW190814) using a density-dependent relativistic mean field model (DD-RMF). This simple, yet powerful formalism provides the freedom necessary to fulfill simultaneously nuclear and astrophysical constraints. The results obtained from the TOV equations show that the hyperons soften the EoS, lowering the maximum mass of NS to around $2.2 M_\odot$, thereby satisfying more conservative massive constraints from the astrophysical observations. The radius of the NS canonical mass is seen to be insensitive to the appearance of hyperons. Both the nucleonic and the hyperonic stars satisfy the constraints from mass-radius limits inferred from NICER observations and tidal deformability constraints from the LIGO and VIRGO collaborations.

5. Summary and Conclusion

We modeled massive nucleonic and hyperonic stars that fulfill the constraints set by the observation of the possibly most massive

Table 6. Stellar properties: Maximum mass (M_{max}), corresponding radius (R_{max}), canonical mass radius ($R_{1.4}$), and dimensionless tidal deformability ($\Lambda_{1.4}$) of hyperonic star for the DD-MEX EoS at different values of the parameter α_v without magnetic field and with magnetic field with different values of the magnetic dipole moment.

μ (Am ²)	$\alpha_v=0.75$				$\alpha_v=0.50$				$\alpha_v=0.25$			
	M_{max} (M_\odot)	R (km)	$R_{1.4}$ (km)	$\Lambda_{1.4}$	M_{max} (M_\odot)	R (km)	$R_{1.4}$ (km)	$\Lambda_{1.4}$	M_{max} (M_\odot)	R (km)	$R_{1.4}$ (km)	$\Lambda_{1.4}$
0	2.217	12.335	13.168	791.483	2.239	12.335	13.168	791.483	2.283	12.453	13.168	791.483
5×10^{30}	2.240	12.543	13.213	815.398	2.271	12.632	13.224	869.281	2.316	12.652	13.237	914.012
5×10^{31}	2.349	13.522	14.741	1338.714	2.366	13.708	14.821	1397.389	2.407	13.563	14.938	1425.185
10^{32}	2.437	13.995	14.992	1510.783	2.480	14.224	15.069	1615.288	2.556	14.469	15.403	1879.880

We also studied the effects of strong magnetic fields on DD-RMF nucleonic and hyperonic EoSs. We investigated the EoS and particle populations using a realistic chemical potential-dependent magnetic field that was developed by solving Einstein-Maxwell equations. For very strong magnetic fields, the spherical symmetric solutions obtained by solving the TOV equations lead to an overestimation of the mass and the radius and, hence, cannot be used for determining stellar properties. For this reason, we used the LORENE library to determine stellar properties of magnetic NSs. For low values of the magnetic dipole moment, implying lower strengths of magnetic fields, the EoS resembles the non-magnetic one. For higher magnetic dipole moments, the EoS stiffens at higher energy density. The amount of stiffness is larger in case of hyperonic EoSs than for the case of pure nucleonic ones. As the magnetic field strength is increased, the particle fractions of leptons (e^- and μ^-) increases at higher densities and the appearance of charged hyperons (Ξ^-) is delayed.

The stiffening in the EoS caused by the changes in population described above increases the maximum mass of magnetic stars. For a small dipole moment of 5×10^{30} Am², the nucleonic and hyperonic mass-radius profiles resemble the non-magnetic case due to the lower magnetic field produced. For higher magnetic dipole moments, although the variation in the maximum mass is small, a variation of about 1 km is seen in the radius of the NS canonical mass. For hyperonic stars, the maximum mass increases by $\approx 0.3 M_\odot$, allowing them to satisfy the GW190814 possible mass constraint for a dipole moment $\mu \geq 10^{32}$ Am² when different coupling schemes are considered. For strong magnetic fields, the different coupling schemes for hyperons predict increases in radius of $\approx 0.2 - 1$ km. Thus, we see that different hyperon couplings and different hyperon potentials populate stellar matter differently and, hence, can change stellar properties significantly.

The change in the dimensionless tidal deformability for NS was studied. It was found that, for higher value of the magnetic dipole moment, the tidal deformability of the canonical mass surpasses the upper limit of 800 set by the measurement from GW170817, which is consistent with the acknowledgement of such objects possessing weak magnetic fields. No such measurement of tidal deformability is available for GW190814, as it has no tidal signatures. But if in the future, measurements of tidal deformability of massive NSs such as the one measured for the secondary object in GW190814 are ≤ 800 , this would imply that object could not be a hyperonic magnetar.

In the future, we will investigate the effect of considering more exotic particles in our modelling of magnetic NSs. These include, kaons, Δ -resonances and deconfined quark matter (with and without mixtures of phases). We also intend to analyze combined effects of magnetic fields and fast rotation on stars containing exotic matter, as both of these aspects could be important in young stars (Lasky et al. 2019; Yu et al. 2019; Lasky et al. 2017).

Acknowledgements. AAU acknowledges the Inter-University Centre for Astronomy and Astrophysics, Pune, India for support via an associateship and for hospitality. VD thanks Valentina Sarti for useful discussions and acknowledges support from the National Science Foundation under grant PHY-1748621 and PHAROS (COST Action CA 16214).

References

Abbott, B. P., Abbott, R., et al. 2017, Phys. Rev. Lett., 119, 161101
 Abbott, B. P., Abbott, R., et al. 2018, Phys. Rev. Lett., 121, 161101
 Abbott, B. P., Abbott, R., et al. 2019, Phys. Rev. X, 9, 011001
 Abbott, R., Abbott, T. D., et al. 2020, Astrophys. Jour., 896, L44
 Aguirre, R. M. 2019, Phys. Rev. C, 100, 065203
 Aguirre, R. M. 2020, Phys. Rev. D, 102, 096025
 Ambartsumyan, V. A. & Saakyan, G. S. 1960, Sov. Astron., 4, 187
 Antoniadis, J. & Freire *et al.*, P. C. C. 2013, Science, 340
 Avancini, S. S., Brito, L., Marinelli, J. R., et al. 2009, Phys. Rev. C, 79, 035804
 Avancini, S. S., Dexheimer, V., Farias, R. L. S., & Timóteo, V. S. 2018, Phys. Rev. C, 97, 035207
 Baldo, M., Burgio, G. F., & Schulze, H. J. 2000, Phys. Rev. C, 61, 055801
 Bandyopadhyay, D., Chakrabarty, S., & Pal, S. 1997, Phys. Rev. Lett., 79, 2176
 Banik, S. & Bandyopadhyay, D. 2001, Phys. Rev. C, 64, 055805
 Banik, S., Hempel, M., & Bandyopadhyay, D. 2014, Astrophys. Jour. Suppl. Ser., 214, 22
 Baym, G., Pethick, C., & Sutherland, P. 1971, Astrophys. J., 170, 299
 Beloborodov, A. M. 2020, Astrophys. Jour., 896, 142
 Beniamini, P., Wadiasingh, Z., & Metzger, B. D. 2020, MNRAS, 496, 3390
 Bhowmick, B., Bhattacharya, M., Bhattacharyya, A., & Gangopadhyay, G. 2014, Phys. Rev. C, 89, 065806
 Biswas, B. & Bose, S. 2019, Phys. Rev. D, 99, 104002
 Biswas, B., Nandi, R., Char, P., Bose, S., & Stergioulas, N. 2020, GW190814: On the properties of the secondary component of the binary
 Bocquet, M., Bonazzola, S., Gourgoulhon, E., & Novak, J. 1995, Astron. Astrophys., 301, 757
 Bombaci, I., Drago, A., Logoteta, D., Pagliara, G., & Vidaña, I. 2020, Was GW190814 a black hole – strange quark star system?
 Bonazzola, S. & Gourgoulhon, E. 1996, Astron. Astrophys., 312, 675
 Bonazzola, S., Gourgoulhon, E., Salgado, M., & Marck, J. A. 1993, Astron. Astrophys., 278, 421
 Bransgrove, A., Levin, Y., & Beloborodov, A. 2017, MNRAS, 473, 2771
 Brockmann, R. & Toki, H. 1992, Phys. Rev. Lett., 68, 3408
 Broderick, A., Prakash, M., & Lattimer, J. M. 2000, Astrophys. Jour., 537, 351
 Cardall, C. Y., Prakash, M., & Lattimer, J. M. 2001, Astrophys. Jour., 554, 322
 Casali, R. H., Castro, L. B., & Menezes, D. P. 2014, Phys. Rev. C, 89, 015805
 Chakrabarty, S., Bandyopadhyay, D., & Pal, S. 1997, Phys. Rev. Lett., 78, 2898
 Chatterjee, D., Elghozi, T., Novak, J., & Oertel, M. 2015, MNRAS, 447, 3785
 Chatterjee, D. & Vidaña, I. 2016, Eur. Phys. J. A, 52, 29
 Chatterjee, D. & Vidaña, I. 2016, Eur. Phys. Jour. A, 52, 29
 Chen, W.-C. & Piekarewicz, J. 2015, Phys. Rev. Lett., 115, 161101
 Christian, J.-E. & Schaffner-Bielich, J. 2021, Phys. Rev. D, 103, 063042
 Ciolfi, R., Kastaun, W., Kalinani, J. V., & Giacomazzo, B. 2019, Phys. Rev. D, 100, 023005
 Colucci, G. & Sedrakian, A. 2014, J. Phys. Conf. Ser., 496, 012003
 Cromartie, H. T. & Fonseca *et al.*, E. 2019, Nature Astron., 4, 72
 Danielewicz, P. & Lee, J. 2014, Nucl. Phys. A, 922, 1
 Demircik, T., Ecker, C., & Järvinen, M. 2021, Astrophys. J. Lett., 907, L37
 Demorest, P. B., Pennucci, T., Ransom, S. M., Roberts, M. S. E., & Hessels, J. W. T. 2010, Nature, 467, 1081
 Dexheimer, V., Franzon, B., Gomes, R., et al. 2017, Phys. Lett. B, 773, 487
 Dexheimer, V., Gomes, R. O., Klähn, T., Han, S., & Salinas, M. 2021, Phys. Rev. C, 103, 025808

Dexheimer, V., Negreiros, R., & Schramm, S. 2012, *Eur. Phys. J. A.*, 48, 189

Dexheimer, V. & Schramm, S. 2008, *Astrophys. J.*, 683, 943

DHapo, H., Schaefer, B.-J., & Wambach, J. 2010, *Phys. Rev. C*, 81, 035803

Dhiman, S. K., Kumar, R., & Agrawal, B. K. 2007, *Phys. Rev. C*, 76, 045801

Dover, C. & Gal, A. 1984, *Prog. Part. and Nucl. Phys.*, 12, 171

Fattoyev, F. J., Horowitz, C. J., Piekarewicz, J., & Reed, B. 2020, *Phys. Rev. C*, 102, 065805

Fattoyev, F. J., Piekarewicz, J., & Horowitz, C. J. 2018, *Phys. Rev. Lett.*, 120, 172702

Felipe, R. G., Martinez, A. P., Rojas, H. P., & Orsaria, M. 2008, *Phys. Rev. C*, 77, 015807

Fortin, M., Avancini, S. S., Providência, C., & Vidaña, I. 2017, *Phys. Rev. C*, 95, 065803

Fortin, M., Raduta, A. R., Avancini, S., & Providência, C. 2020, *Phys. Rev. D*, 101, 034017

Fortin, M., Raduta, A. R., Avancini, S., & Providência, C. 2021, *Phys. Rev. D*, 103, 083004

Frieben, J. & Rezzolla, L. 2012, *Mon. Not. Roy. Astron. Soc.*, 427, 3406

Gendreau, K. C., Arzoumanian, Z., et al. 2016, in *Society of Photo-Optical Instrumentation Engineers (SPIE) Conference Series*, Vol. 9905, *Space Telescopes and Instrumentation 2016: Ultraviolet to Gamma Ray*, ed. J.-W. A. den Herder, T. Takahashi, & M. Bautz, 99051H

Giacomazzo, B., Zrake, J., Duffell, P., MacFadyen, A. I., & Perna, R. 2015, *Astrophys. J.*, 809, 39

Glendenning, N. K. 1982, *Phys. Lett. B*, 114, 392

Glendenning, N. K. 1985, *Astrophys. Jour.*, 293, 470

Glendenning, N. K. 2001, *Phys. Rev. C*, 64, 025801

Glendenning, N. K. & Moszkowski, S. A. 1991, *Phys. Rev. Lett.*, 67, 2414

Godzieba, D. A., Radice, D., & Bernuzzi, S. 2021, *Astrophys. J.*, 908, 122

Gomes, R. O., Dexheimer, V., Schramm, S., & Vasconcellos, C. A. Z. 2015, *Astrophys. J.*, 808, 8

Gomes, R. O., Franzon, B., Dexheimer, V., & Schramm, S. 2017, *Astrophys. J.*, 850, 20

Gomes, R. O., Pais, H., Dexheimer, V., Providência, C., & Schramm, S. 2019, *Astron. Astrophys.*, 627, A61

Goncalves, V. P. & Lazzari, L. 2020, *Phys. Rev. D*, 102, 034031

Guichon, P. A. M., Stone, J. R., & Thomas, A. W. 2018, *Prog. Part. Nucl. Phys.*, 100, 262

Gupta, A., Gerosa, D., Arun, K. G., et al. 2020, *Phys. Rev. D*, 101, 103036

Gusakov, M. E., Haensel, P., & Kantor, E. M. 2014, *Mon. Not. Roy. Astron. Soc.*, 439, 318

Harada, T. & Hirabayashi, Y. 2006, *Nucl. Phys. A*, 767, 206

Harada, T. & Hirabayashi, Y. 2015, *Phys. Lett. B*, 740, 312

Harding, A. K. & Lai, D. 2006, *Rep. Prog. Phys.*, 69, 2631

Haskell, B., Samuelsson, L., Glampedakis, K., & Andersson, N. 2008, *Mon. Not. Roy. Astron. Soc.*, 385, 531

Hinderer, T. 2008, *Astrophys. J.*, 677, 1216

Hinderer, T., Lackey, B. D., Lang, R. N., & Read, J. S. 2010, *Phys. Rev. D*, 81, 123016

Huang, K., Hu, J., Zhang, Y., & Shen, H. 2020a, *Astrophys. Jour.*, 904, 39

Huang, K., Hu, J., Zhang, Y., & Shen, H. 2020b, *Astrophys. J.*, 904, 39

Huang, X.-G., Huang, M., Rischke, D. H., & Sedrakian, A. 2010, *Phys. Rev. D*, 81, 045015

Hulse, R. A. & Taylor, J. H. 1975, *Astrophys. Jour. Lett.*, 195, L51

Inoue, T. 2019a, *JPS Conf. Proc.*, 26, 023018

Inoue, T. 2019b, *AIP Conf. Proc.*, 2130, 020002

Isaka, M., Yamamoto, Y., & Rijken, T. A. 2017, *Phys. Rev. C*, 95, 044308

Jiang, W.-Z., Li, B.-A., & Fattoyev, F. J. 2015, *Eur. Phys. Jour. A*, 51, 161101

Kaspi, V. M. & Beloborodov, A. M. 2017, *Ann. Rev. Astron. Astrophys.*, 55, 261

Khadikar, S., Raduta, A. R., Oertel, M., & Sedrakian, A. 2021, Maximum mass of compact stars from gravitational wave events with finite-temperature equations of state

Khalilov, V. R. 2002, *Phys. Rev. D*, 65, 056001

Klevansky, S. P. 1992, *Rev. Mod. Phys.*, 64, 649

Kumar, B., Biswal, S. K., & Patra, S. K. 2017, *Phys. Rev. C*, 95, 015801

Lalazissis, G. A., Nikšić, T., Vretenar, D., & Ring, P. 2005, *Phys. Rev. C*, 71, 024312

Lasky, P. D., Leris, C., Rowlinson, A., & Glampedakis, K. 2017, *Astrophys. J. Lett.*, 843, L1

Lasky, P. D., Sarin, N., & Ashton, G. 2019, *AIP Conf. Proc.*, 2127, 020025

Lattimer, J. M. & Prakash, M. 2007, *phys. rep.*, 442, 109

Lattimer, J. M. & Prakash, M. 2016, *Phys. Rep.*, 621, 127, memorial Volume in Honor of Gerald E. Brown

Lattimer, J. M. & Steiner, A. W. 2014, *Astrophys. Jour.*, 784, 123

Levin, Y., Beloborodov, A. M., & Bransgrove, A. 2020, *Astrophys. Jour.*, 895, L30

Li, B.-A. & Han, X. 2013, *Phys. Lett. B*, 727, 276

Li, J. J., Long, W. H., & Sedrakian, A. 2018a, *Eur. Phys. Jour. A*, 54, 133

Li, J. J. & Sedrakian, A. 2019a, *Phys. Rev. C*, 100, 015809

Li, J. J. & Sedrakian, A. 2019b, *Astrophys. Jour.*, 874, L22

Li, J. J., Sedrakian, A., & Weber, F. 2018b, *Phys. Lett. B*, 783, 234

Li, J. J., Sedrakian, A., & Weber, F. 2020, *Phys. Lett. B*, 810, 135812

Lim, Y., Bhattacharya, A., Holt, J. W., & Pati, D. 2020a

Lim, Y., Bhattacharya, A., Holt, J. W., & Pati, D. 2020b, Radius and equation of state constraints from massive neutron stars and GW190814

Lopes, L. L. & Menezes, D. P. 2014, *Phys. Rev. C*, 89, 025805

Lopes, L. L. & Menezes, D. P. 2018, *JCAP*, 05, 038

Lopes, L. L. & Menezes, D. P. 2021, *Nucl. Phys. A*, 1009, 122171

LORENE. -, *Langage Objet pour la RElativité NumériquE*, <http://www.lorene.obspm.fr>

Mallick, R. & Schramm, S. 2014, *Phys. Rev. C*, 89, 045805

Margalit, B., Beniamini, P., Sridhar, N., & Metzger, B. D. 2020, *Astrophys. Jour.*, 899, L27

Mereghetti, S., Pons, J. A., & Melatos, A. 2015, *Space Sci. Rev.*, 191, 315

Miller *et al.*, M. C. 2019, *Astrophys. J.*, 887, L24

Most, E. R., Papenfort, L. J., & Rezzolla, L. 2019, *Mon. Not. Roy. Astron. Soc.*, 490, 3588

Most, E. R., Papenfort, L. J., Weih, L. R., & Rezzolla, L. 2020, *MNRAS*, 499, L82

Nikšić, T., Vretenar, D., Finelli, P., & Ring, P. 2002, *Phys. Rev. C*, 66, 024306

Oertel, M., Providência, C., Gulminelli, F., & Raduta, A. R. 2015, *J. Phys. G*, 42, 075202

Oppenheimer, J. R. & Volkoff, G. M. 1939, *Phys. Rev.*, 55, 374

Özel, F., Baym, G., & Güver, T. 2010, *Phys. Rev. D*, 82, 101301

Pais, H. & Providência, C. m. c. 2016, *Phys. Rev. C*, 94, 015808

Paulucci, L., Ferrer, E. J., de la Incera, V., & Horvath, J. E. 2013, *IAU Symp.*, 291, 465

Pili, A. G., Bucciantini, N., & Del Zanna, L. 2017, *Mon. Not. Roy. Astron. Soc.*, 470, 2469

Pons, J. A. & Viganò, D. 2019, *Liv. Rev. Comput. Astrophys.*, 5, 3

Rabhi, A., Providência, C., & Da Providência, J. 2008a, *J. Phys. G*, 35, 125201

Rabhi, A., Providência, C., & Providência, J. D. 2008b, *Jour. Phys. G: Nucl. and Part. Phys.*, 35, 125201

Rather, I. A., Ikram, M., & Imran, M. 2018, in *Proceedings of the DAE Symp. on Nucl. Phys.*, Vol. 63, 794

Rather, I. A., Usmani, A., & Patra, S. 2021a, *Nucl. Phys. A*, 1010, 122189

Rather, I. A., Usmani, A. A., & Patra, S. K. 2021b, Hadron-Quark phase transition in the context of GW190814

Raynaud, R., Guilet, J., Janka, H.-T., & Gastine, T. 2020, *Sci. Adv.*, 6, eaay2732

Riahi, R. & Kalantari, S. Z. 2021, *Int. J. Mod. Phys. D*, 30, 2150001

Riley *et al.*, T. E. 2019, *Astrophys. J.*, 887, L21

Roupaas, Z., Panotopoulos, G., & Lopes, I. 2020, QCD color superconductivity in compact stars: color-flavor locked quark star candidate for the gravitational-wave signal GW190814

Schaffner, J., Dover, C., Gal, A., et al. 1994, *Ann. Phys.*, 235, 35

Schaffner, J. & Mishustin, I. N. 1996, *Phys. Rev. C*, 53, 1416

Schaffner-Bielich, J. & Gal, A. 2000, *Phys. Rev. C*, 62, 034311

Sedrakian, A., Weber, F., & Li, J. J. 2020, *Phys. Rev. D*, 102, 041301

Sen, D., Banerjee, K., & Jha, T. K. 2018, *Int. Jour. Mod. Phys. E*, 27, 1850097

Shahrbaf, M., Blaschke, D., Grunfeld, A. G., & Moshfegh, H. R. 2020, *Phys. Rev. C*, 101, 025807

Spinella, W. M. & Weber, F. 2019, *Astron. Nachr.*, 340, 145

Sur, A. & Haskell, B. 2021, *Mon. Not. Roy. Astron. Soc.*, 502, 4680

Tan, H., Noronha-Hostler, J., & Yunes, N. 2020, *Phys. Rev. Lett.*, 125, 261104

Taninah, A., Agbemava, S., Afanasjev, A., & Ring, P. 2020, *Phys. Lett. B*, 800, 135065

Tews, I., Pang, P. T. H., Dietrich, T., et al. 2021, *Astrophys. J. Lett.*, 908, L1

Thapa, V. B. & Sinha, M. 2020, *Phys. Rev. D*, 102, 123007

Thapa, V. B., Sinha, M., Li, J. J., & Sedrakian, A. 2020, *Part. C*, 3, 660

Tolman, R. C. 1939, *Phys. Rev.*, 55, 364

Tolos, L., Centelles, M., & Ramos, A. 2016, *Astrophys. Jour.*, 834, 3

Tolos, L., Centelles, M., & Ramos, A. 2017, *Astrophys. J.*, 834, 3

Tolos, L., & Fabbietti, L. 2020, *Prog. Part. Nucl. Phys.*, 112, 103770

Tsokaros, A., Ruiz, M., & Shapiro, S. L. 2020, *Astrophys. J.*, 905, 48

Turola, R., Zane, S., & Watts, A. L. 2015, *Rep. Prog. Phys.*, 78, 116901

Typel, S. & Wolter, H. 1999, *Nucl. Phys. A*, 656, 331

Vidaña, I. 2018, *Proc. Roy. Soc. Lond. A*, 474, 0145

Vidaña, I. 2013, *Nucl. Phys. A*, 914, 367, *xI International Conference on Hyper-nuclear and Strange Particle Physics (HYP2012)*

Wei, B., Zhao, Q., Wang, Z.-H., et al. 2020, *Ch. Phys. C*, 44, 074107

Wu, X., Bao, S., Shen, H., & Xu, R. 2021, Symmetry energy effect on the secondary component of GW190814 as a neutron star

Xue, Y. Q. et al. 2019, *Nature*, 568, 198

Yakhshiev, U., Kim, H.-C., & Oka, M. 2019, *Phys. Rev. D*, 99, 054027

Yu, Y.-W., Chen, A., Dai, Z.-G., et al. 2019, *AIP Conf. Proc.*, 2127, 020024

Zanazzi, J. J. & Lai, D. 2020, *Astrophys. Jour.*, 892, L15

Zhang, N.-B. & Li, B.-A. 2020, *Astrophys. Jour.*, 902, 38

Zhang, Y., Liu, M., Xia, C.-J., Li, Z., & Biswal, S. K. 2020, *Phys. Rev. C*, 101, 034303

Zhong, S.-Q. & Dai, Z.-G. 2020, *Astrophys. J.*, 893, 9

Zhou, X., Li, A., & Li, B.-A. 2021, *Astrophys. J.*, 910, 62

Zhu, Z., Li, A., & Rezzolla, L. 2020, *Phys. Rev. D*, 102, 084058

Özel, F. & Freire, P. 2016, *Ann. Rev. Astron. and Astrophys.*, 54, 401

Appendix A:

Within the relativistic density-dependent mean field (DD-RMF) model, the equation of motion for baryons obtained by applying the Euler Lagrange equations to the Lagrangian density (1) is written as

$$\sum_B \left[i\gamma_\mu D^\mu - \gamma^0 \left(g_\omega(\rho_B) \omega + \frac{1}{2} g_\rho(\rho_B) \rho \tau_3 + \sum_R (\rho_B) \right) - M_B^* \right] \psi_B = 0, \quad (\text{A.1})$$

where, $M_B^* = M_B - g_\sigma(\rho_B) \sigma$ is the effective mass of baryons and \sum_R is the rearrangement term due to the density dependence of the coupling constants

$$\sum_R (\rho_B) = -\frac{\partial g_\sigma}{\partial \rho_B} \sigma \rho_s + \frac{\partial g_\omega}{\partial \rho_B} \omega \rho_B + \frac{1}{2} \frac{\partial g_\rho}{\partial \rho_B} \rho \rho_3. \quad (\text{A.2})$$

The equation of motion for meson fields are

$$\begin{aligned} m_\sigma^2 \sigma &= g_\sigma(\rho_B) \rho_s, \\ m_\omega^2 \omega &= g_\omega(\rho_B) \rho_B, \\ m_\rho^2 \rho &= \frac{g_\rho(\rho_B)}{2} \rho_3, \end{aligned} \quad (\text{A.3})$$

where the scalar density ρ_s , baryon density ρ_B , and isovector densities ρ_{s3} , and ρ_3 , are given as

$$\begin{aligned} \rho_s &= \sum_B \bar{\psi} \psi, \\ \rho_B &= \sum_B \psi^\dagger \psi, \\ \rho_{s3} &= \sum_B \bar{\psi} \tau_3 \psi, \\ \rho_3 &= \sum_\alpha \psi^\dagger \tau_3 \psi = \rho_p - \rho_n. \end{aligned} \quad (\text{A.4})$$

With the above equations, the expression for the energy density and pressure are

$$\begin{aligned} \mathcal{E}_m &= \sum_B \frac{2}{(2\pi)^3} \int_0^{k_B} d^3 k E_B^*(k) + \frac{1}{2} m_\sigma^2 \sigma^2 - \frac{1}{2} m_\omega^2 \omega^2 - \frac{1}{2} m_\rho^2 \rho^2 \\ &\quad + g_\omega(\rho_B) \omega \rho_B + \frac{g_\rho(\rho_B)}{2} \rho \rho_3, \\ P_m &= \sum_B \frac{2}{3(2\pi)^3} \int_0^{k_B} d^3 k \frac{k^2}{E_B^*(k)} - \frac{1}{2} m_\sigma^2 \sigma^2 + \frac{1}{2} m_\omega^2 \omega^2 \\ &\quad + \frac{1}{2} m_\rho^2 \rho^2 - \rho_B \sum_R (\rho_B), \end{aligned} \quad (\text{A.5})$$

where, $E_B^* = \sqrt{k_B^2 + M_B^{*2}}$. The rearrangement term $\sum_R (\rho_B)$ contributes to the pressure only.

In the presence of magnetic field, the scalar and vector density for charged baryons cb , uncharged baryons ub , and leptons follow

as (Broderick et al. 2000)

$$\begin{aligned} \rho_s^{cb} &= \frac{|q_{cb}| B M_{cb}^{*2}}{2\pi^2} \sum_{v=0}^{v_{max}} r_v \ln \left(\frac{k_{F,v}^{cb} + E_F^{cb}}{\sqrt{M_{cb}^{*2} + 2v|q_{cb}|B}} \right), \\ \rho_s^{ub} &= \frac{M_{ub}^{*2}}{2\pi^2} \left[E_F^{ub} k_F^{ub} - M_{ub}^{*2} \ln \left(\frac{k_F^{ub} + E_F^{ub}}{M_{ub}} \right) \right], \\ \rho_s^{cb} &= \frac{|q_{cb}| B}{2\pi^2} \sum_{v=0}^{v_{max}} r_v k_{F,v}^{cb}, \\ \rho^{ub} &= \frac{(k_F^{ub})^3}{3\pi^2}, \\ \rho_l &= \frac{|q_l| B}{2\pi^2} \sum_{v=0}^{v_{max}} r_v k_{F,v}^l, \end{aligned} \quad (\text{A.6})$$

where r_v is the Landau degeneracy of v level. The expressions for the baryon and lepton energy densities in the presence of magnetic field become

$$\begin{aligned} \mathcal{E}_{cb} &= \frac{|q_{cb}| B}{4\pi^2} \sum_{v=0}^{v_{max}} r_v \\ &\quad \times \left[k_{F,v}^{cb} E_F^{cb} + (M_{cb}^{*2} + 2v|q_{cb}|B) \ln \left(\frac{k_{F,v}^{cb} + E_F^{cb}}{\sqrt{M_{cb}^{*2} + 2v|q_{cb}|B}} \right) \right], \\ \mathcal{E}_{ub} &= \frac{1}{8\pi^2} \left[k_F^{ub} (E_F^{ub})^3 + (k_F^{ub})^3 E_F^{ub} - M_{ub}^{*4} \ln \left(\frac{k_F^{ub} + E_F^{ub}}{M_{ub}^*} \right) \right], \\ \mathcal{E}_l &= \frac{|q_l| B}{4\pi^2} \sum_{v=0}^{v_{max}} r_v \\ &\quad \times \left[k_{F,v}^l E_F^l + (m_l^2 + 2v|q_l|B) \ln \left(\frac{k_{F,v}^l + E_F^l}{\sqrt{m_l^2 + 2v|q_l|B}} \right) \right]. \end{aligned} \quad (\text{A.7})$$